Journal of
Medical Imaging

MedicalImaging.SPIEDigitalLibrary.org

Optimization of beam quality for photon-counting spectral computed tomography in head imaging: simulation study

Han Chen
Cheng Xu
Mats Persson
Mats Danielsson

SPIE.

Journal of Medical Imaging 2(4), 043504 (Oct–Dec 2015)

Optimization of beam quality for photon-counting spectral computed tomography in head imaging: simulation study

Han Chen,* Cheng Xu, Mats Persson, and Mats Danielsson
Royal Institute of Technology (KTH), Department of Physics, Stockholm 106 91, Sweden

Abstract. Head computed tomography (CT) plays an important role in the comprehensive evaluation of acute stroke. Photon-counting spectral detectors, as promising candidates for use in the next generation of x-ray CT systems, allow for assigning more weight to low-energy x-rays that generally contain more contrast information. Most importantly, the spectral information can be utilized to decompose the original set of energy-selective images into several basis function images that are inherently free of beam-hardening artifacts, a potential advantage for further improving the diagnosis accuracy. We are developing a photon-counting spectral detector for CT applications. The purpose of this work is to determine the optimal beam quality for material decomposition in two head imaging cases: nonenhanced imaging and K-edge imaging. A cylindrical brain tissue of 16-cm diameter, coated by a 6-mm-thick bone layer and 2-mm-thick skin layer, was used as a head phantom. The imaging target was a 5-mm-thick blood vessel centered in the head phantom. In K-edge imaging, two contrast agents, iodine and gadolinium, with the same concentration (5 mg/mL) were studied. Three parameters that affect beam quality were evaluated: kVp settings (50 to 130 kVp), filter materials ($Z = 13$ to 83), and filter thicknesses [0 to 2 half-value layer (HVL)]. The image qualities resulting from the varying x-ray beams were compared in terms of two figures of merit (FOMs): squared signal-difference-to-noise ratio normalized by brain dose ($\mathrm{SDNR}^2/\mathrm{BD}$) and that normalized by skin dose ($\mathrm{SDNR}^2/\mathrm{SD}$). For nonenhanced imaging, the results show that the use of the 120-kVp spectrum filtered by 2 HVL copper ($Z = 29$) provides the best performance in both FOMs. When iodine is used in K-edge imaging, the optimal filter is 2 HVL iodine ($Z = 53$) and the optimal kVps are 60 kVp in terms of $\mathrm{SDNR}^2/\mathrm{BD}$ and 75 kVp in terms of $\mathrm{SDNR}^2/\mathrm{SD}$. A tradeoff of 65 kVp was proposed to lower the potential risk of skin injuries if a relatively long exposure time is necessarily performed in the iodinated imaging. In the case of gadolinium imaging, both SD and BD can be minimized at 120 kVp filtered with 2 HVL thulium ($Z = 69$). The results also indicate that with the same concentration and their respective optimal spectrum, the values of $\mathrm{SDNR}^2/\mathrm{BD}$ and $\mathrm{SDNR}^2/\mathrm{SD}$ in gadolinium imaging are, respectively, around 3 and 10 times larger than those in iodine imaging. However, since gadolinium is used in much lower concentrations than iodine in the clinic, iodine may be a preferable candidate for K-edge imaging. *© 2015 Society of Photo-Optical Instrumentation Engineers (SPIE)* [DOI: 10.1117/1.JMI.2.4.043504]

Keywords: photon counting; spectral computed tomography; material decomposition; K-edge imaging.

Paper 15107RR received May 20, 2015; accepted for publication Oct. 9, 2015; published online Nov. 6, 2015.

1 Introduction

Stroke is caused by the interruption of the blood supply to the brain due to the blocking of vessels by a thrombus (ischemic stroke) or vessel bursting (hemorrhagic stroke).[1] According to the World Stroke Organization, 15 million people worldwide are affected by stroke each year; of these, 5 million die and another 5 million are permanently disabled.[2] Of all strokes, ischemic stroke accounts for ~87% of cases and is an important cause of mortality.[3] The major treatment for acute ischemic stroke is the use of intravenous thrombolytic therapy, which has been demonstrated as an effective intervention within 3 h of the onset of symptoms.[4] Another treatment for acute ischemic stroke is the mechanical removal of thrombuses, namely, thrombectomy, which has been drawing more and more attention in recent years.[5–7] Prior to both treatments, a rapid head imaging is necessarily performed to obtain useful information for confirming the diagnosis and aiding the planning of the treatments. Head imaging has two major modalities, x-ray computed tomography (CT) and magnetic resonance imaging (MRI). Compared to MRI, head CT has the advantages of wide availability, low cost, and, most importantly, short acquisition time.

Typically, a comprehensive CT protocol for acute stroke consists of an unenhanced CT, CT angiography (CTA), and sometimes CT perfusion (CTP).[8,9] Unenhanced head CT scanning is the first-line diagnostic test that is performed on all patients with stroke symptoms in order to exclude hemorrhage and extensive infarction, for which the thrombolytic treatment is not beneficial. However, unenhanced CT is limited by the sensitivity (40% to 70%) to ischemic changes.[10] Therefore, CTP and CTA should be performed after unenhanced CT.[11,12] By tracking a contrast agent (which is typically iodine) injected into blood, CTP can be used to obtain physiological information about the cerebral blood flow, cerebral blood volume, and mean transit time. The information can be interpreted to evaluate the size of the infarcted area and distinguish the salvageable tissue

---

*Address all correspondence to: Han Chen, E-mail: hanchen@kth.se

2329-4302/2015/$25.00 © 2015 SPIE

(penumbra) that is at risk of infarction.[13] CTA is usually combined with CTP to determine the vascular anatomy and thrombus positions.[12]

Although the head CT plays an important role in guiding acute stroke management, a major concern is the resulting radiation dose to patients. It has been reported that the dose delivered by a comprehensive CT acute stroke protocol is six times larger than that of a single unenhanced head CT.[8] According to the linear-no-threshold model, such an amount of radiation implies six times the potential risk of cancer. The deterministic skin effect caused by overexposure is rare in acute stroke imaging,[8] but there is one report of hair loss for patients undergoing multiple CTA and CTP.[14] Many researchers have made extensive efforts to reduce the radiation exposure in head CT imaging. Smith et al.[15] implemented a dose modulation technique in which the tube current is automatically adjusted during the CT scan to keep an acceptable noise level. Kalender et al.[16] compared the performance of CTP between 80 and 120 kVp settings and showed that 80 kVp reduced the dose by a factor of 2.8 without decreasing the contrast. Heavy beam filtration is usually recommended to prevent skin injuries, and its effects on image quality have been studied previously.[17,18]

The radiation dose can also be reduced by improving the image quality with new detector technologies. Photon-counting detectors are attracting attention for use in the next generation of x-ray CT. Compared to the conventional energy-integrating CT in which each photon is weighted proportional to the deposited energy, the photon-counting spectral detector is capable of detecting individual photons and sorting them into different energy bins. Because the contrast information is generally greater at low energies, more weight can be assigned to low-energy x-rays.[19,20] Some recent studies have demonstrated that photon-counting spectral detectors with optimal energy weighting improve the signal-difference-to-noise ratio (SDNR) by 10% to 45% compared to energy-integrating detectors at the same patient dose.[21,22] However, the beam-hardening artifacts resulting from energy weighting become more severe,[23] which would to some extent degrade the diagnosis accuracy. An alternative method of utilizing the spectral information obtained by photon-counting detectors is to decompose the original set of energy-selective images into several basis function images using a method called material decomposition,[24,25] where the energy-dependent attenuation coefficient in each pixel is decomposed into a linear combination of several energy-dependent basis functions. Since the basis function images are naturally energy independent, the beam-hardening artifacts can be completely removed in theory, giving a potential advantage in improving the diagnostic accuracy. Moreover, this method opens up new possibilities for quantitative imaging of contrast agents by making use of the K-edge discontinuity of their attenuation curves[26] (i.e., K-edge imaging). The quantitative information of the contrast agents allows for more accurate evaluation in CTP and better identification of thrombuses in CTA. Additionally, in diagnostic procedures requiring pre- and/or postcontrast images, multiple exposures can be avoided, offering a lower dose and less misregistration caused by patient movement between exposures. We are developing an energy-resolving photon-counting silicon-strip detector for CT applications. The previously published measurements on a single detector module have shown high count rate linearity with only 1% count loss at an incident photon flux of 300 M photons $\mathrm{s}^{-1}\,\mathrm{mm}^{-1}$,[27] an RMS energy resolution varying from 1.5 keV for 40 keV photons to 1.9 keV for 100 keV photons,[28] and a temperature stability of 0.1 keV threshold variation per kelvin at 30 keV.[29] The simulation study by Bornefalk and Danielsson[30] shows that by applying the energy-weighting scheme, our silicon detector can perform on par with ideal energy-integrating detectors for routine imaging tasks. The feasibility of using our detector for K-edge imaging has been performed with a single detector module in a table-top laboratory setup, and the results show that the detector has the potential for quantitative measurement of substance concentrations.[31]

Now, we are assembling a full CT detector in a gantry. One of the most concerning issues is to optimize the systematic parameters, especially the beam quality. The purpose of this work is to determine the optimal beam quality for material decomposition in two head imaging cases: nonenhanced imaging and K-edge imaging. A simulation study was performed to compare the image quality relative to the dose received by the head phantom with a wide range of kVp settings, filter materials, and filter thicknesses. The structure of this paper is as follows. In Sec. 2, an analytical framework and figures of merit (FOMs) used for the evaluation of image quality in material decomposition are presented. We describe the detector module and simulation setup in Sec. 3.1. In Sec. 3.2, Monte Carlo simulations are described to calculate the relevant FOMs. The results are shown in Sec. 4 and discussed in Sec. 5.

2 Theory

2.1 *Physical Model for Material Decomposition*

Material decomposition for CT imaging can be performed by two different methods: projection-space decomposition and image-space decomposition. In the former method, the original set of energy-selective images for each CT projection is decomposed into different basis function images before CT reconstruction,[32] while the latter one involves material decomposition based on the reconstructed images acquired by different energy bins.[33] Both of them have been applied to photon-counting CT.[25,34] In this work, we used projection-space basis material decomposition since it allows for a complete elimination of beam-hardening artifacts.

Assuming that a photon-counting spectral detector has N energy bins and x-rays detected by the detector are allocated into different bins according to their deposited energies, the expected number of detected events in bin i for one image projection is given by

$$\lambda_i = \int_0^{\mathrm{keV}_{\max}} \mathrm{d}_x \mathrm{d}_y \,\mathrm{FF}\Phi(E) D(E) S_i(E) \mathrm{e}^{-\int_s \mu(x,y;E)\mathrm{d}s} \mathrm{d}E + \varepsilon_i, \tag{1}$$

where FF is the fill factor of detector pixels with the size of $d_x \times d_y$, $\Phi(E)$ is the energy distribution of the unattenuated spectrum in the detector plane in units of $\mathrm{ph/mm^2}$, $\mathrm{keV}_{\max}$ is the maximum energy of incident x-rays, $D(E)$ is the detection efficiency of the detector, and $\mu(x, y; E)$ is the energy-dependent linear attenuation coefficient in an irradiated object. The sensitivity function $S_i(E)$ describes the probability of an interacting x-ray with the original energy E being detected by bin i; the sensitivity function is determined by

$$S_i = \int_{T_i}^{T_{i+1}} R(E', E)\mathrm{d}E', \tag{2}$$

where T_i and T_{i+1} are the lower and upper thresholds of bin i, respectively, and $R(E', E)$ is the response function giving the probability that an x-ray with original energy E produces an event with deposited energy E'. The last term ε_i in Eq. (1) accounts for the fraction of detected events in bin i from object scattering.

The first step of projection-space material decomposition involves the decomposition of the attenuation coefficient $\mu(x, y; E)$ into a linear combination of m known energy-dependent basis functions f_α for each x-ray path through the object:

$$\mu(x, y; E) = \sum_{\alpha=1}^{m} a_\alpha(x, y) f_\alpha(E), \quad \alpha = 1, \dots, m, \tag{3}$$

where $a_\alpha(x, y)$ refers to the composition of basis material α at position (x, y) on the x-ray path. Equation (1) can then be rewritten as a function of the line integrals of a_α along the x-ray path s, $A_\alpha = \int_s a_\alpha(x, y)\mathrm{d}s$:

$$\lambda_i(A_1, A_2, \dots, A_m) = \int_0^{\mathrm{kVp_{max}}} \mathrm{d}_x \mathrm{d}_y \, \mathrm{FF}\Phi(E) D(E) R_i(E) \mathrm{e}^{-\sum_{\alpha=1}^{m} A_\alpha(x) f_\alpha(E)} \mathrm{d}E. \tag{4}$$

Let $n_i (i = 1, \dots, N)$ be the outcome observed in the energy bin i for one image projection. The second step involves the use of the observed outcome n_i in each energy bin to determine the line integral A_α. We apply the maximum likelihood approach for the estimation of A_α, as discussed by Roessl and Proksa.[26] Assuming that N energy bins are independent of each other and the output from each energy bin follows a Poisson distribution with mean value λ_i, line integrals A_α are estimated by maximizing likelihood function P, given one measurement $\{n_1, \dots, n_N\}$:

$$\hat{A}_1, \hat{A}_2, \dots, \hat{A}_m = \arg\max \mathrm{P}(n_1, \dots, n_N | \lambda_1, \lambda_2, \dots, \lambda_N), \tag{5}$$

where

$$\mathrm{P}(n_1, \dots, n_N | \lambda_1, \lambda_2, \dots, \lambda_N) = \prod_{i=1}^{N} \frac{\lambda_i^{n_i}}{n_i!} \mathrm{e}^{-\lambda_i}. \tag{6}$$

In practice, it is often more convenient to minimize the negative logarithm of the likelihood function:

$$\begin{aligned} \hat{A}_1, \hat{A}_2, \dots, \hat{A}_m &= \arg\min[-\ln(\mathrm{P})] \\ &= \arg\min \sum_{i}^{N} (\lambda_i - n_i \ln \lambda_i). \end{aligned} \tag{7}$$

The lowest covariance between estimators $\hat{A}_\alpha$ and $\hat{A}_\beta$ can be calculated with the aid of the Cramer–Rao lower bound:[35]

$$\mathrm{Cov}(\hat{A}_\alpha, \hat{A}_\beta) \geq (\mathrm{F}^{-1})_{\alpha\beta}, \tag{8}$$

where F is the Fisher information matrix with its elements given by

$$\mathrm{F}_{\alpha\beta} = \sum_{i=1}^{N} \frac{1}{\lambda_i} \frac{\partial \lambda_i}{\partial A_\alpha} \frac{\partial \lambda_i}{\partial A_\beta}. \tag{9}$$

After solving Eq. (7) for $\hat{A}_\alpha$ for all x-ray paths in each projection, m basis function images representing the distributions of their respective compositions over the object are generated separately using reconstruction algorithms. According to the theoretical work by Hanson,[36] a single-pixel variance σ_r^2 in a reconstructed image is equal to the variance σ_p^2 of a projection measurement at that pixel multiplied by a constant:

$$\sigma_r^2 = \frac{\sigma_p^2}{p^2 M_\theta} k^2, \tag{10}$$

where p is the spacing between two neighboring projection measurements, M_θ is the total projection number, and k is a unitless factor related to a filter kernel used in the image reconstruction and determined to be $k = 0.62$ for MATLAB's iradon function with the cropped Ram–Lak ramp filter.[37] By substituting Eqs. (8) into (10), the lowest covariance between $\hat{a}_\alpha$ and $\hat{a}_\beta$ for each reconstructed voxel is obtained:

$$\mathrm{Cov}(\hat{a}_\alpha, \hat{a}_\beta) = \frac{\mathrm{Cov}(\hat{A}_\alpha, \hat{A}_\beta)}{p M_\theta} k^2 \geq \frac{\mathrm{F}_{\alpha\beta}^{-1}}{p M_\theta} k^2. \tag{11}$$

2.2 *Figure of Merit*

Statistical decision theory, which is based on hypothesis testing, is extensively used to optimize the image quality in medical imaging.[38–40] A comprehensive description of this theory can be found in the publication by Barrett and Myers [41] To apply the theory to our photon-counting spectral imaging system, we assume two hypotheses, H_0 and H_1, representing the absence and presence of an imaging target, respectively. The task is then defined as deciding whether the imaging target is present or not. In the following, we consider two imaging cases: nonenhanced imaging and K-edge imaging.

In the absence of a contrast agent, the attenuation of an object can be accurately described by a linear combination of either contributions from Compton scattering and the photoelectric effect or the attenuation coefficients of two basis materials with a distinct difference in the average atomic number.[42] In this work, we use the latter decomposition manner, taking the attenuation coefficients of bone μ_{bo} and soft tissue μ_{st} as basis functions:

$$\mu(x, y; E) = a_{\mathrm{bo}}(x, y)\mu_{\mathrm{bo}}(E) + a_{\mathrm{st}}(x, y)\mu_{\mathrm{st}}(E). \tag{12}$$

Let $\hat{\mathbf{a}}$ be a 1×2 vector $\hat{\mathbf{a}} = (\hat{a}_{\mathrm{bo}}, \hat{a}_{\mathrm{st}})$, with entries being the estimated values of a_α for $\alpha \in \{\mathrm{bo}, \mathrm{st}\}$. In order to decide whether the estimated values $\hat{\mathbf{a}}$ belongs to H_0 or H_1, a discriminant function is formed by properly weighting the bone basis image and soft tissue basis image together, based on the ideal linear observer model:

$$T(\hat{\mathbf{a}}) = \mathbf{w}\hat{\mathbf{a}}^T, \tag{13}$$

where $\mathbf{w} = (w_1, w_2)$ is a vector of weighting factors. The outcome of Eq. (13) is then compared to a certain threshold t_c such that the estimated value $\hat{\mathbf{a}}$ will belong to H_0 if $t < t_c$ and to H_1 otherwise. To minimize the risk of making incorrect decisions, the weight vector $\mathbf{w}$ in the discriminant function $T(\hat{\mathbf{a}})$ is optimized in terms of the squared SDNR:

$$\mathrm{SDNR}^2 = \frac{(\mathbf{w}\Delta\mathbf{a}^T)^2}{\mathbf{w}(K^1 + K^0)\mathbf{w}^T}, \tag{14}$$

where K^0 and K^1 are 2×2 symmetric covariance matrices for two hypotheses, respectively, with the entries being $K_{\alpha\beta} = \mathrm{Cov}(\hat{a}_\alpha, \hat{a}_\beta)$; vector $\Delta\mathbf{a} = (\Delta a_{\mathrm{bo}}, \Delta a_{\mathrm{st}})$ describes the differences in the expected values of a_α between two hypotheses. Assuming that the attenuation is uniform in the imaging target as well as in its corresponding background, the entries in $\Delta\mathbf{a}$ can then be calculated as the difference in A_α between two hypotheses divided by the thickness d_t of the imaging target:

$$\Delta\mathbf{a} = \frac{[\Delta A_{\mathrm{bo}}, \Delta A_{\mathrm{st}}]^T}{d_t} = \frac{\Delta\mathbf{A}}{d_t}. \tag{15}$$

Using the theorem of Cauchy–Schwarz inequality, it has been proved that the optimal weighting $\mathbf{w}$ that maximizes the squared SDNR is given by[41]

$$\mathbf{w} = (K^0 + K^1)^{-1}\Delta\mathbf{a}. \tag{16}$$

Therefore, the maximum squared SDNR of the discriminant $T(\hat{\mathbf{a}})$ in the reconstructed domain becomes

$$\mathrm{SDNR}^2 = \Delta\mathbf{a}(K^1 + K^0)^{-1}\Delta\mathbf{a}^T, \tag{17}$$

which can be further written as a function of A_α by substituting Eq. (11) and Eq. (15) into Eq. (17):

$$\mathrm{SDNR}^2 = \frac{p^2 M_\theta}{k^2 d_t^2}\Delta\mathbf{A}(\mathrm{F}^0 + \mathrm{F}^1)\Delta\mathbf{A}^T. \tag{18}$$

In order to correctly describe the energy dependence of the attenuation in the presence of a contrast agent, the decomposition of the linear attenuation in Eq. (12) is extended by adding the attenuation coefficient of the contrast agent as the third basis function:[43,44]

$$\mu(x, y; E) = a_{\mathrm{bo}}(x, y)\mu_{\mathrm{bo}}(E) + a_{\mathrm{st}}(x, y)\mu_{\mathrm{st}}(E) + a_k(x, y)\mu_k(E). \tag{19}$$

In practice, it is more interesting to see the concentration distribution of the contrast agent since its presence and amount can be used to characterize the imaging regions of interest. Therefore, for K-edge imaging, we calculated the squared SDNR in the contrast agent basis image instead of in the combined image:

$$\mathrm{SDNR}^2 = \frac{a_k^2}{\mathrm{Cov}(\hat{a}_k, \hat{a}_k)}, \tag{20}$$

with a_k determined by the line integral A_k divided by the target thickness d_t, that is, A_k/d_t. Substituting Eq. (11) into Eq. (20), the squared SDNR in the reconstruction domain becomes

$$\mathrm{SDNR}^2 = \frac{p^2 M_\theta}{k^2 d_t^2}\frac{A_k^2}{\mathrm{F}_{k,k}^{-1}}. \tag{21}$$

For both nonenhanced imaging and K-edge imaging, the SDNR^2 obtained by varying incident x-ray beams $\Phi(E)$ is normalized by the corresponding dose delivered to the head, an FOM independent of radiation exposure. In this work, two kinds of doses to the head are considered: BD and SD. The former one shows the potential risk of cancer, while the SD is an indicator for skin injuries.

3 Materials and Method

3.1 *Description of Detector and Head Phantom*

A photograph of a single detector module is shown in Fig. 1(a). The detector module is fabricated on a high-resistivity n-type silicon substrate with a thickness of 0.5 mm and consists of

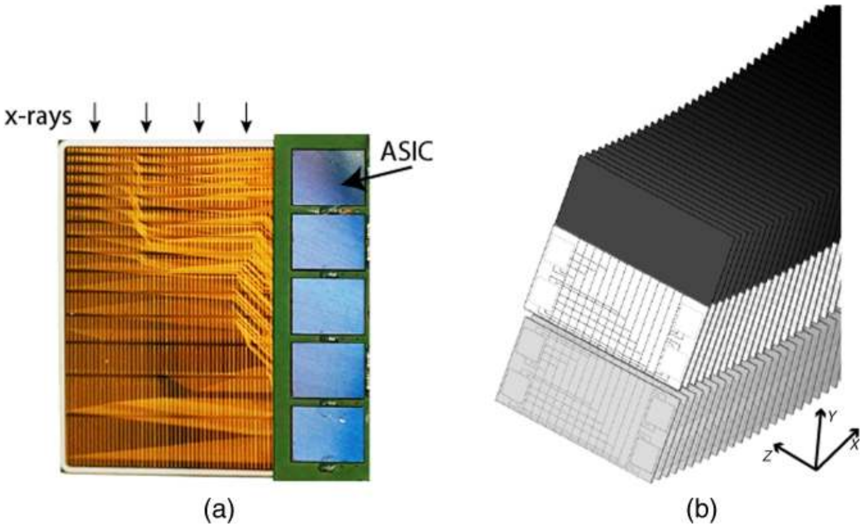

Fig. 1 (a) Photograph of a single detector module. X-rays are incident from the top of the detector module, and the application-specific integrated circuits (ASICs) are located on the right side protected by a thick tungsten slab. (b) Illustration of a full computed tomography (CT) detector with a two-layer design. The detector modules are stacked in two different layers, with the lower detector layer offset by one module thickness along the x-axis relative to the upper layer.

100 detector strips, each with a pitch of 0.4 mm. As a result, a pixel size of 0.5 mm × 0.4 mm is given for each detector strip by orienting the module with its edge directed toward the x-ray beam (i.e., edge-on). The active absorption path along the x-ray incident direction is $l_a = 3$ cm, along with a dead layer of $l_d = 0.6$ mm at the front edge. According to the Lambert–Beer law, the detection efficiency $D(E)$ for x-rays with energy E is calculated as

$$D(E) = \mathrm{e}^{-u_{\mathrm{si}}(E) l_d}(1 - \mathrm{e}^{-u_{\mathrm{si}}(E) l_a}), \tag{22}$$

where $u_{\mathrm{si}}(E)$ is the silicon attenuation coefficient taken from the XCOM database.[45] In order to overcome the problem of high photon fluxes encountered in CT imaging, the detector strip is subdivided into 16 segments along the x-ray incident direction. The segment length is exponentially increased, providing a nearly uniform count rate over all segments. Each segment is connected to an individual electronic readout channel on application-specific integrated circuits (ASICs) bonded directly to the right side of the silicon substrate. The charge produced by x-ray interactions is amplified by the ASICs and subsequently converted into current pulses, with the pulse height proportional to the amount of the corresponding deposited energy. The resulting pulses are compared with eight energy thresholds ($N = 8$) and then sorted into one of the energy bins sided by two neighboring thresholds. More detailed information about the ASIC can be found in earlier publications.[27,46]

Figure 1(b) illustrates the geometry of a full CT detector assembly, which consists of a large number (1500 to 2000) of detector modules. To facilitate the cooling and mounting of electronics, the detector modules are stacked in two different layers, with the lower detector layer offset by one module thickness along the x-axis relative to the upper layer. The backside of each detector module is coated by a 30-μm-thick sheet of tungsten to reduce the scatter radiation between different detector modules, yielding an FF of around 0.97. In order to reject the scatter radiation from objects, the tungsten sheaths at the upper detector layer are extended by 2.5 cm toward the x-ray source, acting as a one-dimensional grid.

Figure 2 shows the schematic of the entire CT gantry with a head phantom located at the isocenter. The source-to-detector distance D_1 is 1000 mm, and the detector-to-isocenter distance D_2 is 500 mm, resulting in a geometric magnification of 2. Spectrum $\Phi(E)$ is produced by a tungsten anode x-ray tube with varying kVp settings and is subsequently filtered by a filter with atomic number Z and thickness l_z. To ensure that the primary x-rays hit the detector surface orthogonally, the entire CT detector is pointed toward the x-ray source and rotates around an axis parallel to the z-axis. The spacing p between two neighboring projection acquisitions is assumed to be equal to the pixel width d_x along the x-axis, giving $M_\theta = \pi D_2 / d_x$ projections over 180-deg rotation.

As for the head phantom studied in this work, a cylindrical brain tissue is assumed, with a diameter of 16 cm and a length of 14 cm, the same size as specified by the Food and Drug Administration for the head CT dose index measurement.[47] To include the effects induced by the skin and the skull, the cylindrical brain phantom is coated by a 6-mm-thick bone layer and 2-mm-thick skin layer. A blood vessel of diameter $d_t = 5$ mm embedded in the center of the phantom volume is assumed as an imaging target. The head phantom is irradiated by a uniformly distributed fan beam with a width of 2 cm along the z-axis at the isocenter. In K-edge imaging, two kinds of contrast agents, iodine and gadolinium, are considered in the blood. Iodine is widely used in CT imaging, but its K-edge absorption energy of 33.2 keV is so low that it becomes difficult to easily observe the K-edge discontinuity in the spectrum after transmitting objects. Additionally, photon starvation might occur in the case of heavy attenuation, making the K-edge discontinuity totally unobservable. Gadolinium, frequently used in MRI, has a higher K-edge absorption energy of 50.2 keV, thus promising an improved image quality. The concentrations of both contrast agents in the blood are assumed to be 5 mg/mL.

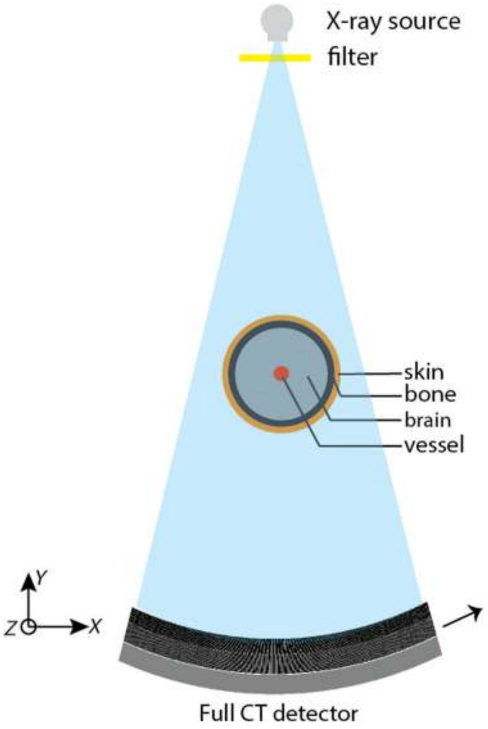

Fig. 2 Schematic of the simulation setup with a full CT detector. The head phantom located at the isocenter is irradiated by an x-ray fan beam with a width of 2 cm, along the z-axis at the isocenter.

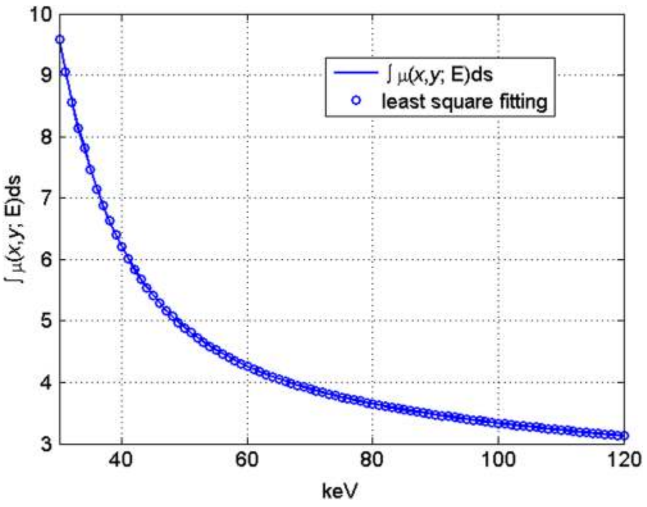

Fig. 3 Total attenuation, $\int \mu(x, y; E)\mathrm{d}s$, for the x-ray path through the phantom center in iodine imaging and its least square fitting with the function $\sum A_\alpha \mu_\alpha$, $\alpha \in \{\mathrm{bo}, \mathrm{st}, \mathrm{Iodine}\}$.

The total attenuation, $\int \mu(x, y; E)\mathrm{d}s$, for the x-ray path through the phantom center is calculated using the attenuation coefficients of different materials taken from the XCOM database.[45] By applying the nonlinear least squares method, the values of A_α are determined by fitting $\int \mu(x, y; E)\mathrm{d}s$ with the function $\sum A_\alpha \mu_\alpha$ ($\alpha \in \{\mathrm{bo}, \mathrm{st}\}$ for nonenhanced imaging and $\alpha \in \{\mathrm{bo}, \mathrm{st}, k\}$ for K-edge imaging. Figure 3 shows an example of the least square fitting in the iodine case. The values of A_α for the x-ray path through the center of the head phantom are summarized in Tables 1 and 2, for nonenhanced and K-edge imaging cases, respectively. The same results can also be obtained by replacing n_i in Eq. (7) with the expected value λ_i and then solving it for A_α.

Table 1 Values of A_α (cm) in nonenhanced imaging under hypothesis H_0: absence of a 5-mm-thick blood vessel, and hypothesis H_1: presence of the blood vessel, and the difference in A_α between two hypotheses.

	H_0	H_1	ΔA_α
A_{bo}	1.2003	1.2019	1.62×10^{-3}
A_{st}	16.1745	16.1794	4.93×10^{-3}

Table 2 Values of A_α (cm) in K-edge imaging for 5 mg/mL iodine and 5 mg/mL gadolinium.

	Iodine	Gadolinium
A_{bo}	1.2019	1.2019
A_{st}	16.1795	16.1795
A_k	5.07×10^{-4}	3.16×10^{-4}

3.2 *Simulation*

3.2.1 *Sensitivity function $S_i(E)$*

As shown in Eq. (2), the sensitivity function $S_i(E)$ of each bin i is determined by the energy response function $R(E', E)$ and the corresponding energy boundaries $[T_i, T_{i+1})$. The energy response function $R(E', E)$ on the full CT detector is calculated by Monte Carlo simulations using Geant4 Application for Tomographic Emission.[48] The monochromatic incident energies ranging from 10 to 130 keV in steps of 1 keV are applied in the simulation. For each keV, 10^6 x-rays uniformly incident on the pixel located at the center of the detector plane are tracked until they escape from the full detector volume. The position information and deposited energies of all the interaction events, including characteristic x-rays produced by the tungsten sheets, are recorded. Figure 4(a) shows an example of the distribution of interaction positions over the detector plane for 80 keV incident x-rays. Because of the tungsten shielding, the reabsorption events caused by Compton scattering along the x-axis are much less than those along the z-axis. In the simulation, it might be possible that the scattered x-rays are reabsorbed in the primary interacting pixel. For such events, we take the sum of their deposited energies. It is well known that if an x-ray interaction occurs near the pixel boundary, the charge cloud produced by its deposited energy will expand to become large enough while drifting across the pixel such that the produced charge will be shared by two or more neighboring pixels, an effect called charge sharing. This effect leads to incomplete charge collection and double counting. For our detector geometry, charge sharing does not occur along the x-axis since charge cannot be shared between different detector modules. The impact of charge sharing on the energy response function $R(E', E)$ is taken into account using the charge collection model presented by Bornefalk and Danielsson.[30] In this model, the charge cloud is assumed to be spherical Gaussian distributed with a standard deviation, depending on the deposited energy and interaction depth in the detector. The charge leaking to neighboring pixels is simply determined by

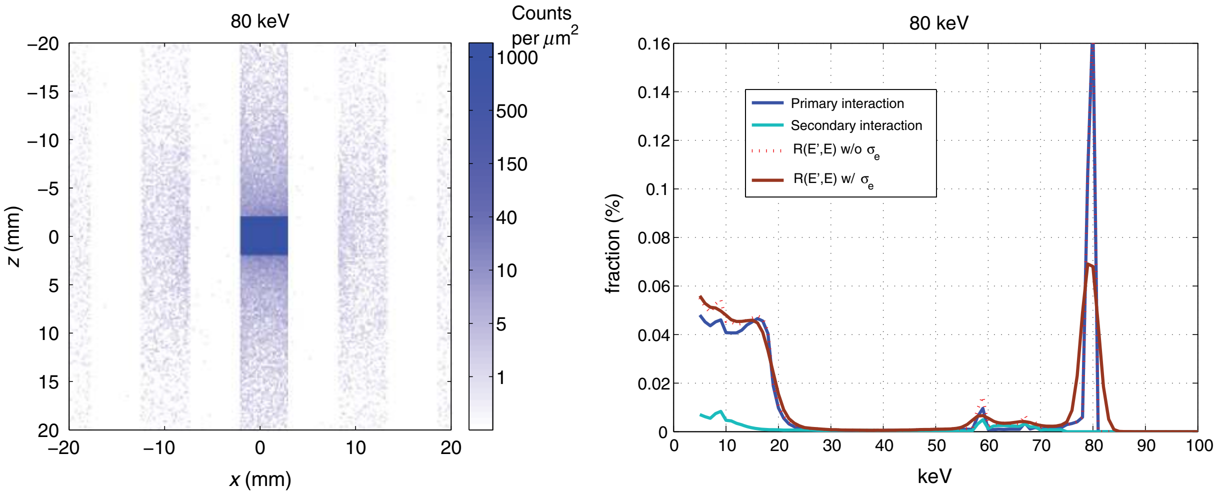

(a)

(b)

Fig. 4 (a) Resulting distribution of interaction positions in the detector plane for 80-keV incident x-rays. (b) Energy distributions of primary (blue line) and secondary (green line) events for 80-keV incident x-rays, and the energy response functions with and without the effect of electronic noise σ_e.

integrating the charge cloud over the neighboring pixel volumes, disregarding the distortion of electric field between the pixels.

The resulting distribution of the initially released energy from the primary interactions for 80 keV x-rays (blue line) is shown in Fig. 4(b). A tail is observed at the low-energy region since a considerable fraction of the x-rays are Compton scattered and deposit a small amount of energy in the original interaction positions. Also shown is the energy distribution of the secondary events (green line) produced by x-rays scattered from the pixel with primary interactions or charge leaking to neighboring pixels. The peaks at around 59 and 67 keV in the curves are due to the characteristic x-rays produced by the tungsten sheets. Assuming that all the pixels in the detector plane show a uniform response to x-rays, the response function $R(E', E)$ for 80 keV x-rays is then determined by adding together the energy distributions of the primary and secondary interactions [red dotted line shown in Fig. 4(b)]. It is inevitable that the detected energy will be altered by electronic noise. In order to include this effect, $R(E', E)$ is modified by convolving it with a Gaussian distribution with a standard deviation of electronic noise, $\sigma_e = 1.1$ keV, measured on a single detector module in an earlier work:[27]

$$R'(E', E) = R(E', E) \otimes \frac{1}{\sigma_e\sqrt{2\pi}} \mathrm{e}^{-\frac{E'^2}{2\sigma_e^2}}. \tag{23}$$

The resulting energy response function $R'(E', E)$ for x-rays with energy ranging between 10 and 130 keV is depicted in Fig. 5(a). The energy distribution as observed by the detector for a broad incident spectrum can be obtained by appropriately weighting together the energy response function of each keV energy. An example of 80 kVp is shown in Fig. 5(b), in comparison with the ideal case, where only photoelectric absorption on the detector is considered. It indicates that the Compton and photoelectric events are well separated, with Compton events being observed <30 keV and photoelectric events >30 keV. The Compton events hence do not destroy the energy information contained in the photoelectric part of the energy distribution.

Although the energy thresholds for computational purposes are not fully optimized in this work, they are set in an arrangement as described below. The first threshold is set at 5 keV to completely remove the false events produced by electronic noise and the second threshold at a value such that the Compton and photoelectric events are well separated [e.g., 30 keV for 80 kVp shown in Fig. 5(b)], while the other six thresholds are equidistantly placed between the second threshold and the maximum energy of the incident spectrum. Roessl and Proksa[26] showed that the SDNR in the gadolinium basis image is significantly increased if one energy threshold is tuned to its K-edge absorption energy. Therefore, in our K-edge imaging study, we set one of the six thresholds closest to the K-edges of the contrast agents at 33 keV for iodine and 50 keV for gadolinium.

After determining the energy response function $R'(E', E)$ and the energy threshold arrangement, the sensitivity function $S_i(E)$ of each bin i can then be determined.

3.2.2 *Dose*

The dose to the head phantom is also determined using Monte Carlo simulations by applying a series of monochromatic x-rays. A fan beam based on the simulation setup is assumed, as described in Sec. 3.1. For one CT projection, N_0 ($N_0 = 10^8$) x-ray photons of each keV impinging on the head phantom are tracked to record the interaction positions and the corresponding deposited energies inside the head volume. As an example, Fig. 6 shows the deposited energy distribution of the head phantom as a result of 80-keV irradiation in one projection. The deposited energy in the axial plane [Fig. 6(a)] is gradually decreased along the x-ray incident direction (i.e., negative y-axis). The bone layer receives more energy than the other two materials because of its relatively high density. Also shown is the deposited energy distribution in the coronal plane [Fig. 6(b)]. As seen in the figure, a fraction of the x-rays is scattered and deposits its energies outside the primary radiation area. The average BD for each keV is calculated as the total deposited energy in the brain tissue divided by its mass. However, for the SD, the highest radiation dose on the patient skin (also called peak SD), instead of the average

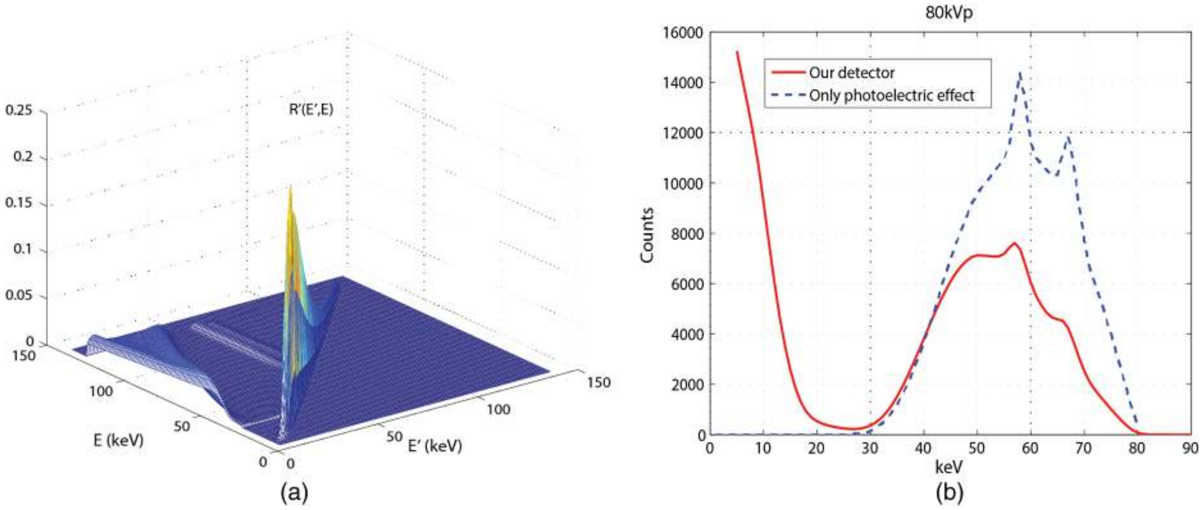

Fig. 5 (a) Energy response function $R'(E', E)$ for x-rays with energy range between 10 and 130 keV. (b) Energy distribution (red line) on the detector for 80 kVp broad spectrum after the passage through the central part of the head phantom. The blue line is for the ideal case where only the photoelectric effect is accounted for.

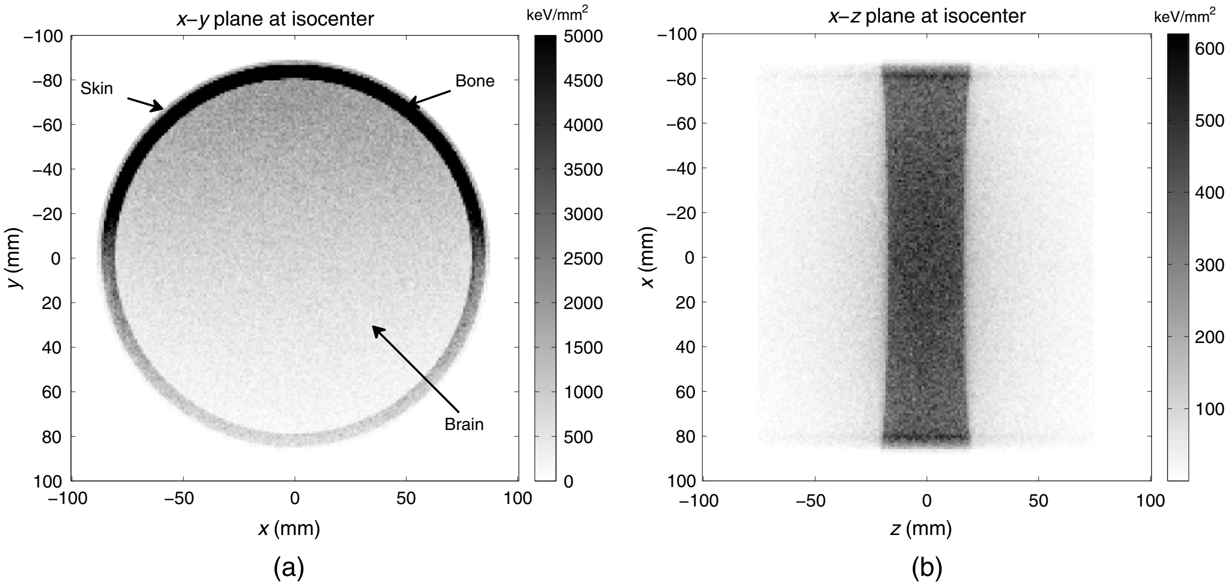

Fig. 6 Distribution of deposited energies over the head phantom in one CT projection for an 80-keV fan beam: (a) in the axial plane (i.e., $x-y$ plane); (b) in the coronal plane (i.e., $x-z$ plane) at the isocenter. The deposited energy is calculated in keV/mm^2 in the planes.

value, is usually used as an indicator to estimate the risk of skin injuries.[49] Therefore, we determine the SD in this work by calculating the deposited energy in a skin volume irradiated by the central part of the fan beam with a width of 1 cm along the z-axis. The resulting values of the BD and SD are plotted as a function of keV in Fig. 7. The BD is gradually increased with keV, while the major contribution to SD is from low energy x-rays, that is, from those with energy between 10 to 40 keV. There is a slight increase in the SD at high keV because of the increasing fraction of Compton scattering.

Given an incident spectrum $\Phi(E)$, the BD for one CT projection is calculated using the following expression:

$$\text{BD} = \int \frac{\text{Dose}(E)}{N_0} \Phi(E)\mathrm{d}E. \tag{24}$$

Because the head phantom is rotationally symmetrical, the resulting dose is the same for all CT projections. The total dose in one CT rotation is then given by a product of the dose per CT projection and the total projection number. Similarly, the SD for one CT rotation can also be calculated.

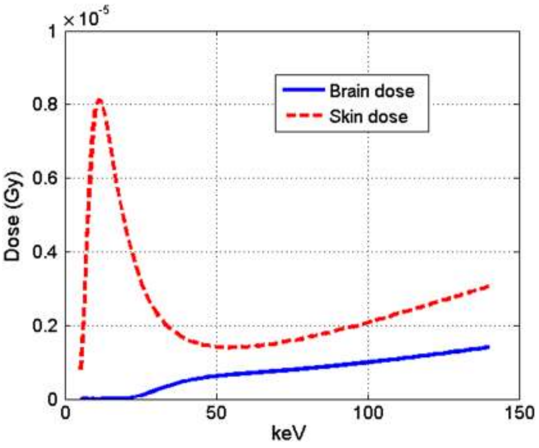

Fig. 7 Brain dose (BD) and skin dose (SD) of the head phantom as a function of keV.

3.2.3 *Object scatter* ε_i

The x-rays that escape from the head phantom are further tracked when reaching the detector plane. Because of the tungsten grid, most of the scattered x-rays are attenuated. The remaining scattered x-rays that pass through the grid will interact with the detector pixels if captured, yielding a scatter image. A primary image can also be obtained by tracking the primary x-rays after passage through the head phantom. To get enough statistics, a region of interest (ROI) of 10×10 pixels centered on the detector plane is selected to calculate the ratio between the number of x-rays scattered from the head phantom and primary x-rays, that is, the scatter-to-primary ratio (SPR). In order to save the computing time, the SPRs for monochromatic x-rays are simulated in steps of 10 keV from 30 to 140 keV, and the results are shown in Fig. 8. The values of SPR for other keV points are obtained through linear interpolation. We assume

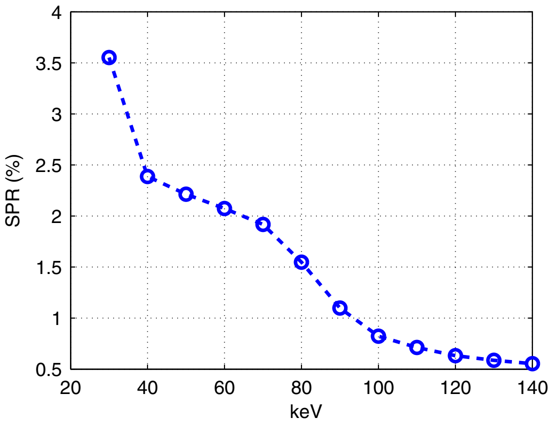

Fig. 8 Scatter-to-primary ratio as a function of keV.

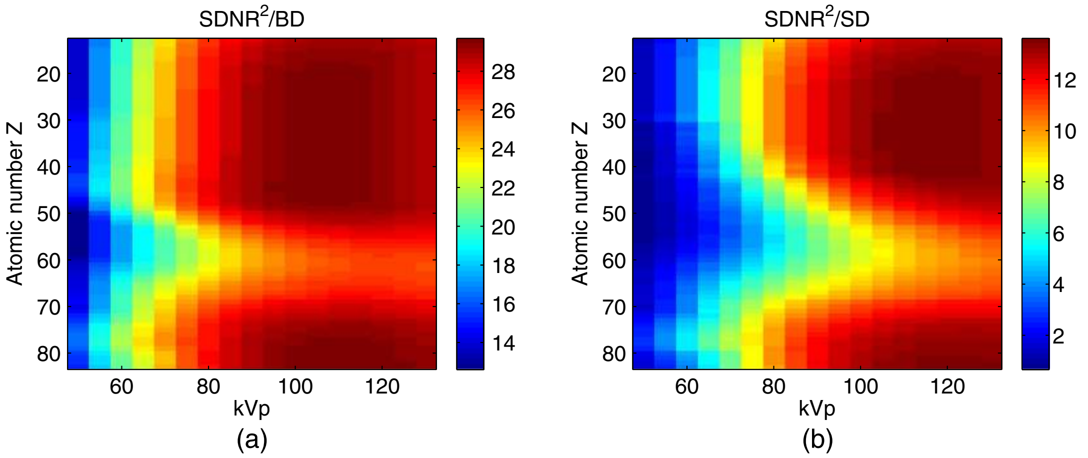

Fig. 9 (a) Brain-dose and (b) skin-dose normalized squared signal-difference-to-noise ratio (SDNR^2) in nonenhanced imaging as a function of kVp and filter material (Z).

that the object scatter has the same response function $R'(E',E)$ as the primary x-rays, disregarding the difference in the incident direction. Therefore, given an incident spectrum, the object scatter ϵ_i detected by bin i at the center of the detector plane is calculated as

$$\epsilon_i = \int \mathrm{SPR}(E)\Phi'(E)S_i(E)\mathrm{d}E, \tag{25}$$

where $\Phi'(E)$ is the spectrum after passing through the central part of the head phantom.

4 Results

The incident spectrum $\Phi(E)$ is varied based on three parameters: kVp settings (50 to 130 kVp), filter materials ($Z = 13$ to 83), and filter thicknesses [$l_z = 0$ to 2 half-value layer (HVL)]. The resulting values of the two FOMs, $\mathrm{SDNR}^2/\mathrm{BD}$, and $\mathrm{SDNR}^2/\mathrm{SD}$, as a function of kVp and filter material for nonenhanced imaging, are shown in Fig. 9, and the corresponding results for K-edge imaging are depicted in Figs. 10 and 11 with iodine and gadolinium, respectively. The filter thickness of each point in Figs. 9–11 is selected such that the FOMs are maximized:

$$l_z^* = \arg\max_{l_z} \mathrm{FOM}(\mathrm{Z}, \mathrm{kVp}, l_z). \tag{26}$$

To clearly show the dependence on the filter material, the FOMs for different imaging cases are plotted as a function of Z in Fig. 12. Again, filter thickness l_Z and kVp for each Z are selected to maximize the FOMs. For nonenhanced imaging [Fig. 12(a)], a minimum region at the atomic number of about $Z = 50$ to 70 is noted, since the corresponding materials have K-edge absorption edges of around 30 to 60 keV above which x-rays are significantly attenuated. A broad maximum region for both FOMs at low atomic numbers ($Z = 20$ to 40) with a peak at copper ($Z = 29$) is observed. In K-edge imaging, both the SD and BD can be minimized at the atomic number of 53 for iodine imaging (middle) and 69 for gadolinium imaging [Fig. 12(b)], which corresponds to the elements iodine and thulium, respectively. Using filter materials with atomic numbers lower or higher than the optimal values will dramatically decrease the FOMs. The results of optimal

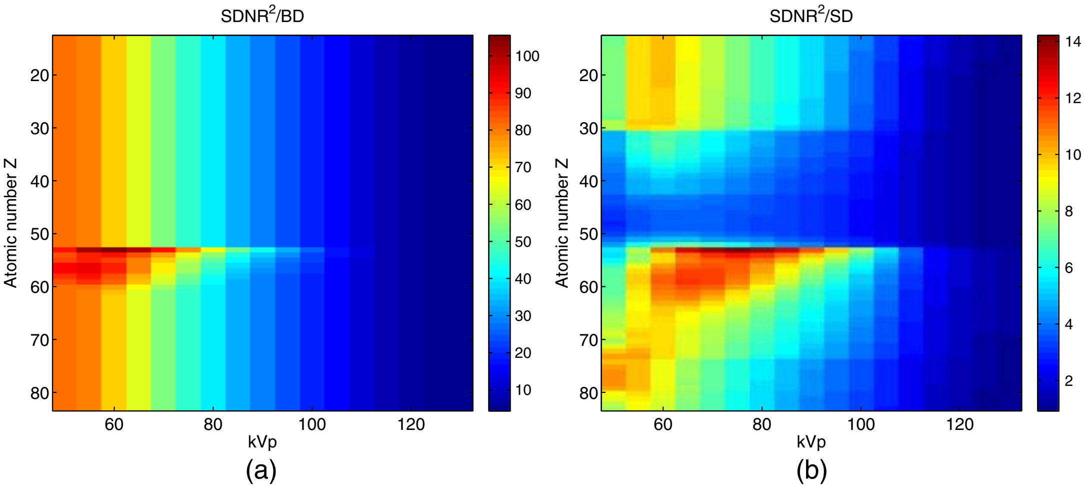

Fig. 10 (a) Brain-dose and (b) skin-dose normalized SDNR^2 as a function of kVp and filter material (Z) in K-edge imaging when iodine is used as a contrast agent.

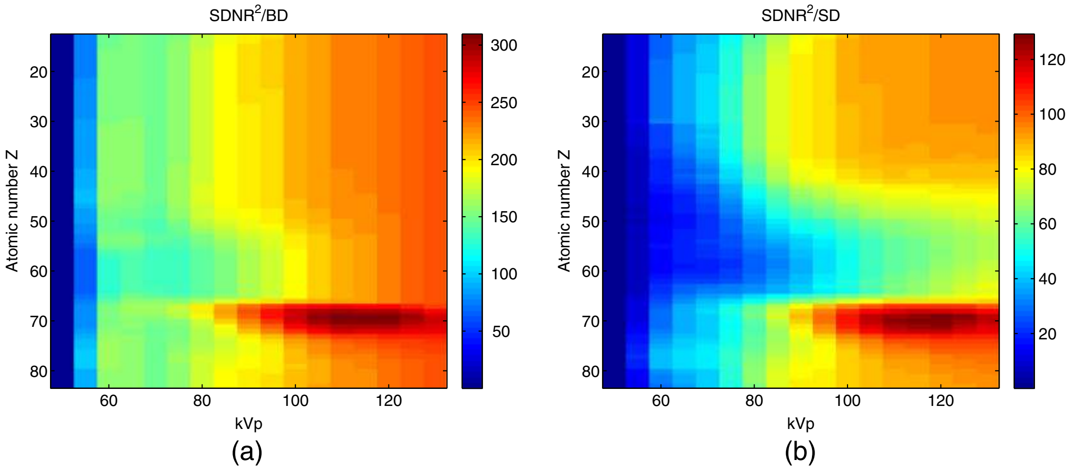

(a) (b)

Fig. 11 (a) Brain-dose and (b) skin-dose normalized SDNR^2 as a function of kVp and filter material (Z) in K-edge imaging when gadolinium is used as a contrast agent.

filters for K-edge imaging can be explained by the fact that the accuracy in the quantification of contrast agents depends on the difference in attenuation to be detected above and below the corresponding K-edges. In iodine imaging, the low K-edge energy of iodine, below which x-rays are heavily attenuated by the head phantom, makes the detection of the K-edge discontinuity more difficult. It is thus important to ensure the accuracy when detecting the low-energy part of the incident spectrum. Using iodine as a filter can not only greatly increase the proportion of x-rays below the K-edge in the incident spectrum but can also attenuate more x-rays above the K-edge such that the energy bin just below the K-edge is less polluted by misregistered events (i.e., high-energy x-rays might be detected by low-energy bins due to charge sharing, electronic noise, or Compton scattering). Unlike iodine, gadolinium has a higher K-edge energy of 50.2 keV, which means that in gadolinium imaging, the accuracy in detecting x-rays below the K-edge is no longer the major factor affecting image quality. Thulium with a K-edge of 59.4 keV, a value close to but higher than that of gadolinium, can highlight the part of the incident spectrum around the K-edge of gadolinium, making the detection of the K-edge discontinuity much easier.

Figure 13 shows the FOMs as a function of thickness l_z of the optimal filters for different imaging cases. For each filter thickness, the kVp setting is chosen to maximize the FOMs. Overall, the FOMs improve with increasing thickness of the optimal filters in all imaging cases. This improvement is more pronounced in SDNR^2/SD in the range of 0 to 1 HVL, because low-energy x-rays, which are the major contribution to SD as illustrated in Fig. 7, are sharply suppressed by the filters. For comparison, the results of the commonly used filter material aluminum are also shown. In nonenhanced imaging, the difference in FOMs between aluminum and the optimal filter copper is small. It is noted in K-edge imaging that SDNR^2/BD is gradually decreased with the increasing thickness of aluminum because of the dramatic loss of x-rays at the low-energy part of the incident spectrum, while SDNR^2/SD is improved with aluminum thickness in the range of 0 to 1 HVL but is insensitive to changes

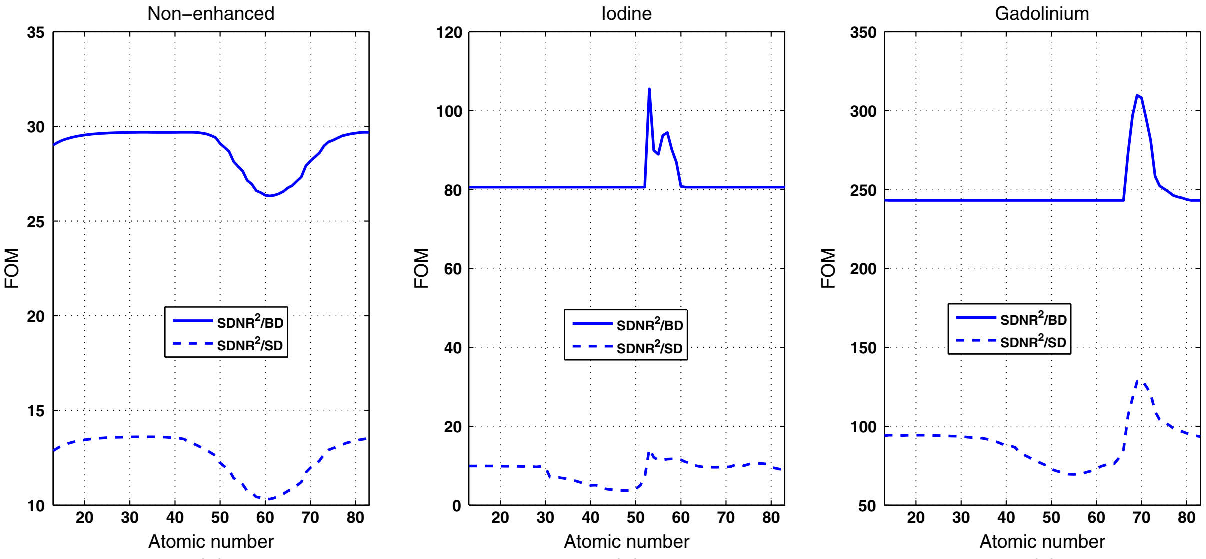

(a) (b) (c)

Fig. 12 Figures of merit (FOMs) as a function of atomic number of filter materials for (a) nonenhanced imaging, (b) K-edge imaging with iodine, and (c) gadolinium.

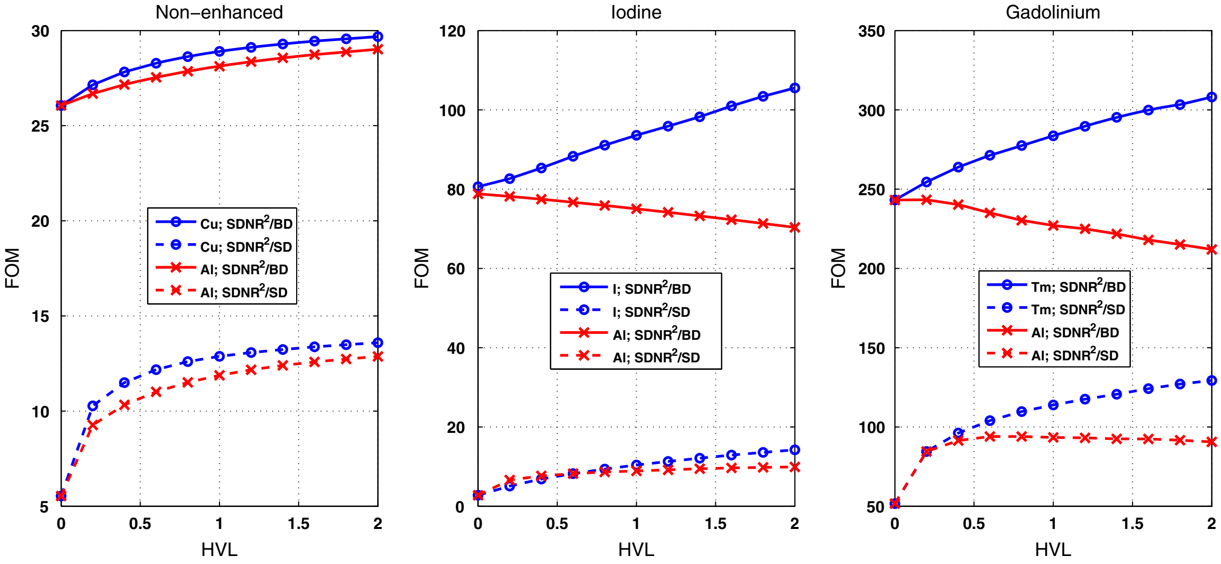

(a) (b) (c)

Fig. 13 FOMs as a function of filter thickness of the optimal filters for (a) nonenhanced imaging, (b) K-edge imaging with iodine, and (c) gadolinium. For comparison, the results for aluminum (Al), the commonly used filter in CT, are also presented (crosses).

in thickness above 1 HVL. Compared to the filter aluminum at the same thickness of 2 HVL, the use of the optimal filters allows for 50% reduction in the BD and 40% reduction in the SD in iodine imaging, 45% reduction in the BD, and 38% reduction in the SD in gadolinium imaging. Further increasing the thickness of the optimal filters beyond 2 HVL can improve the FOMs; however, the heavy filtration requires high tube current to compensate for the flux reduction. Hence, 2 HVL filter thickness is selected for the subsequent evaluations in this work.

Applying 2 HVL optimal filters for nonenhanced and K-edge imaging cases, the resulting FOMs as a function of kVp are shown in Fig. 14 (squares). In nonenhanced imaging, a high kVp setting of 120 kVp is preferred to minimize both the BD and SD. This finding is consistent with the standard clinical operations today and the general conclusion by most researchers[18,50,51] in low-contrast imaging, where the contrast information contained in the x-rays is less energy dependent. Using high kVp settings leads to high transmission through the phantom, thus reducing statistical noise in images. When

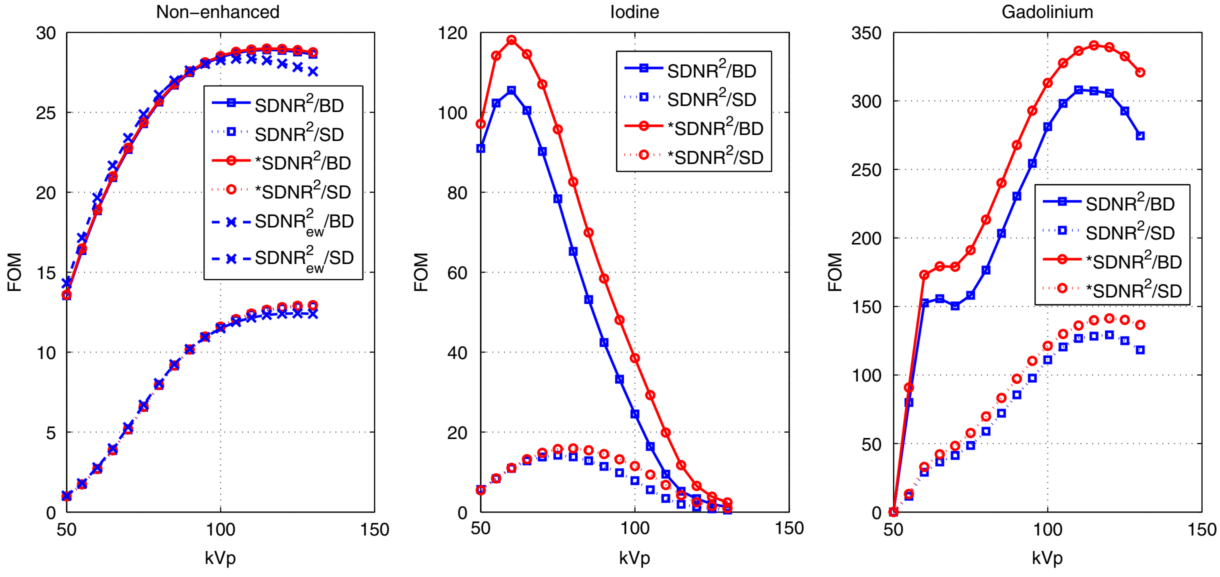

(a) (b) (c)

Fig. 14 Resulting FOMs (squares) as a function of kVp by applying the respective optimal filters of 2 HVL for (a) nonenhanced imaging, (b) K-edge imaging with iodine, and (c) gadolinium. The curves plotted as circles are the results obtained with an assumption that our investigated detector has a large number of energy bins with 1-keV bin width. Also shown in (a) are the results (crosses) obtained using optimal energy weight with the same incident spectrum.

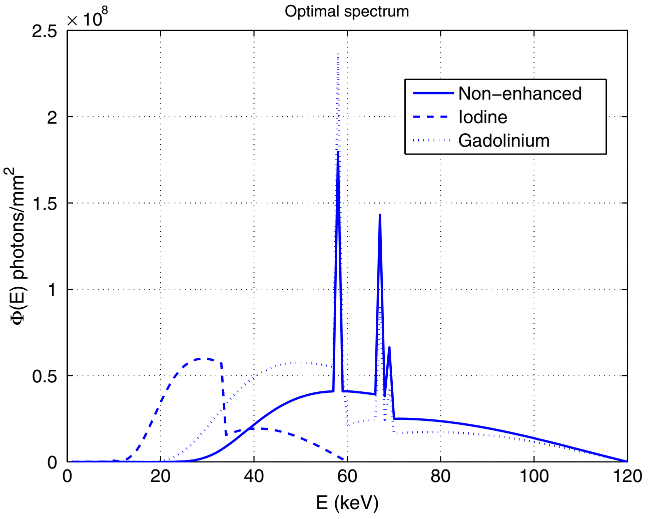

Fig. 15 Resulting optimized incident spectrum $\Phi(E)$ for different imaging cases.

iodine is used in K-edge imaging, the maximum $\mathrm{SDNR}^2/\mathrm{BD}$ is found at 60 kVp, whereas the peak $\mathrm{SDNR}^2/\mathrm{SD}$ is obtained at 75 kVp. It should be noted that the use of 60 kVp leads to a 25% increase in the SD compared to the use of 75 kVp with the same SDNR. For some iodinated head imaging where a relatively long exposure time is required, such as multiple CTA/CTP or interventional CT, in order to lower the potential risk of skin injuries, a tradeoff between the BD and SD can be made by choosing 65 kVp. In gadolinium imaging, the optimal kVp for $\mathrm{SDNR}^2/\mathrm{BD}$ is 120 kVp, the same as that for $\mathrm{SDNR}^2/\mathrm{SD}$. Figure 15 shows the resulting optimized incident spectrum $\Phi(E)$ for different imaging cases. The values of mean energy of the optimal spectrum are 29 and 58 keV for iodine imaging and gadolinium imaging, respectively.

5 Discussion and Conclusions

We have shown an analytical framework to evaluate the CT images resulting from material decomposition. Using this framework, we have optimized the beam quality used for head CT imaging based on our silicon-strip spectral detector. The incident beam was adjusted based on three parameters: kVp setting (50 to 130 kVp), atomic number of filtration ($Z = 13$ to 83), and filter thickness ($l_Z = 0$ to 2 HVL).

For nonenhanced head imaging, we weighted together the two decomposed basis function images, bone and soft tissue, to enhance the detectability of imaging targets. The results show that the use of 120-kVp spectrum filtered by 2 HVL copper provides the best performance in both $\mathrm{SDNR}^2/\mathrm{BD}$ and $\mathrm{SDNR}^2/\mathrm{SD}$ when imaging a 5-mm blood vessel in the head phantom. An advantage of material decomposition is that it is free of beam-hardening artifacts, in contrast to the energy-weighting method. However, it might also be of interest to investigate the difference in image quality between these two methods without considering beam-hardening artifacts. The work by Alvarez[52] shows that with an ideal detector that has infinitesimal energy bin width and perfect energy response, material decomposition provides the same SDNR as optimal energy weighting. To prove that this conclusion also holds for practical detectors, we reanalyzed the simulation data of our silicon-strip detector in this work and calculated the SDNR with optimal energy weighting in a way similar to that described in Sec. 2.2:

$$\mathrm{SDNR}_{\mathrm{ew}}^2 = \frac{p^2 M_\theta}{k^2 d_t^2}\Delta\mathbf{g}(Q^0 + Q^1)^{-1}\Delta\mathbf{g}^T, \tag{27}$$

where $\Delta\mathbf{g}^T$ is a 1×8 column vector with elements Δg_i showing the signal difference in the log-normalized projection image of bin i between the two hypotheses H_0 and H_1, which, in the low-contrast case, is approximated to be the relative difference in the mean values of detected events in that bin: $\Delta\lambda_i/\lambda_i$. Q^m is a 8×8 diagonal matrix for hypothesis H_m, with the diagonal element $Q_{i,i}^m$ referring to the variance in bin i after log-normalization, which is equal to the inverse of λ_i.[36] Using the same filter of 2 HVL copper, we showed that the resulting dose-normalized $\mathrm{SDNR}_{\mathrm{ew}}^2$ plotted as crosses in Fig. 14(a) is similar to those obtained using material decomposition. Further comparison of the two image formation methods involving the effect of beam-hardening artifacts will be investigated in future work.

For K-edge imaging, iodine and gadolinium were studied with the same concentration in the blood vessel, namely, 5 mg/mL. The SDNR in the contrast agent basis image was calculated and normalized by the corresponding dose for

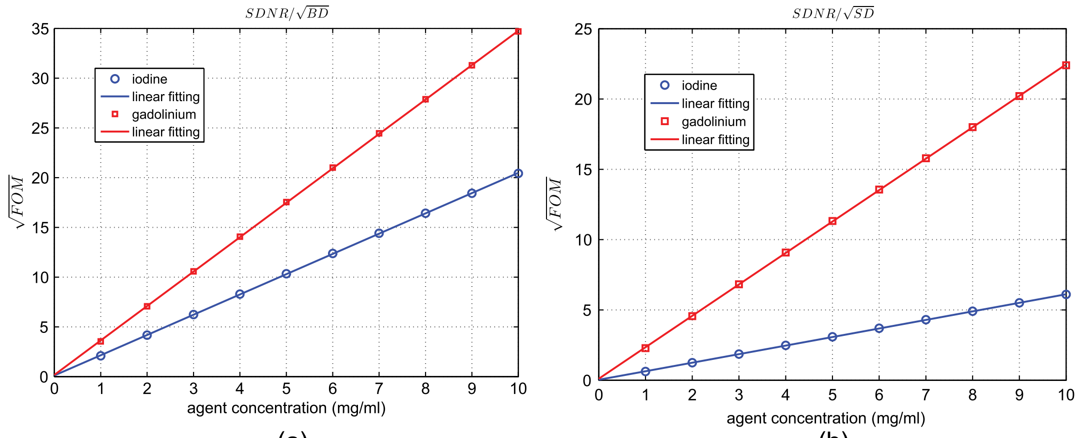

(a) (b)

Fig. 16 Square roots of the FOMs as a function of agent concentration for both iodine and gadolinium imaging, with their respective optimal spectrum obtained at the agent concentration of 5 mg/mL. (a) $\mathrm{SDNR}/\sqrt{\mathrm{BD}}$ and (b) $\mathrm{SDNR}/\sqrt{\mathrm{SD}}$.

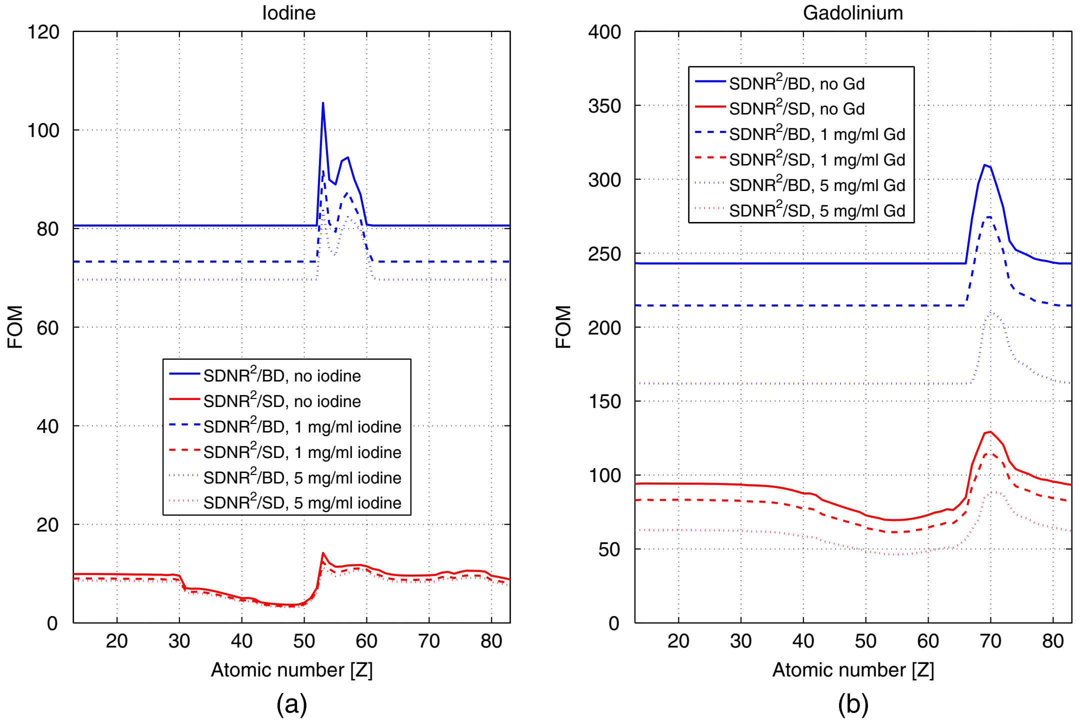

Fig. 17 Resulting FOMs as a function of atomic number (Z) of filter materials for K-edge imaging when the contrast agents of two different concentrations, 1 mg/mL (dashed line) and 5 mg/mL (dotted line), are present in the brain tissue, in comparison with those (solid line) obtained without the contrast agents in the brain tissue. Note that the filter thickness and kVp for each atomic number are determined to maximize the FOMs, as shown in Fig. 12.

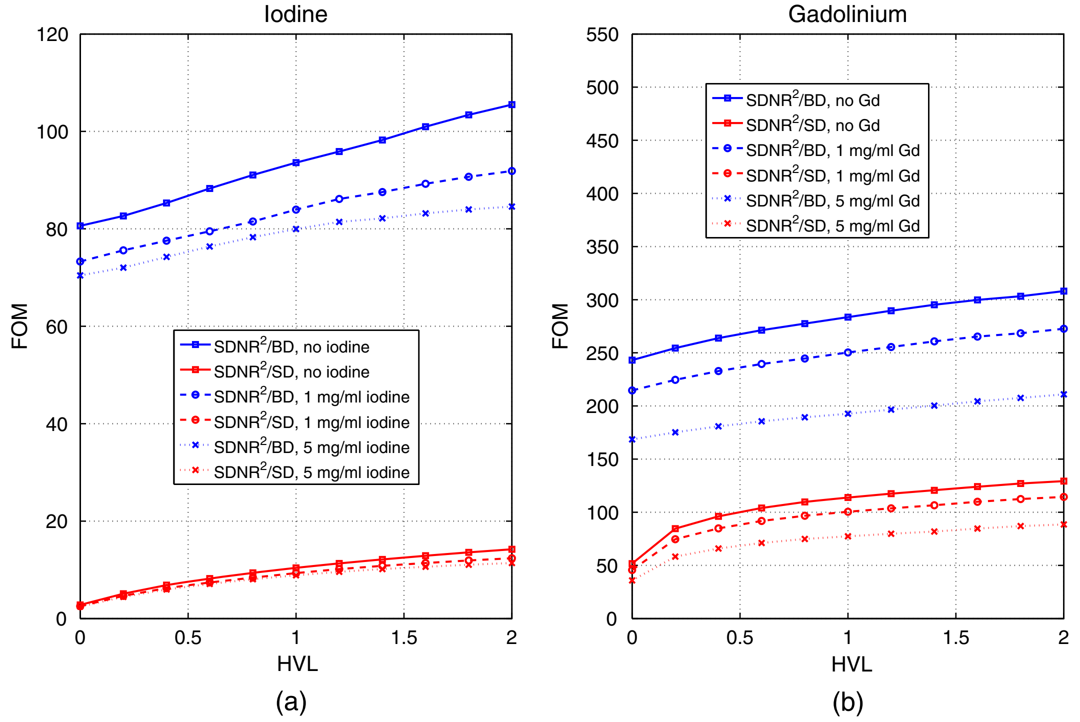

Fig. 18 FOMs as a function of filter thickness (l_Z) of the optimal filters (iodine for iodine imaging and thulium for gadolinium imaging), when the contrast agents of two different concentrations, 1 mg/mL (circles) and 5 mg/mL (crosses), are present in the brain tissue.

each incident spectrum. The results indicate that when iodine is used, the optimal filter is 2 HVL iodine and the optimal kVps are 60 and 75 kVp in terms of $\mathrm{SDNR}^2/\mathrm{BD}$ and $\mathrm{SDNR}^2/\mathrm{SD}$, respectively, while in the gadolinium case, both the SD and BD can be minimized by using 120 kVp filtered with 2 HVL thulium. Using the obtained optimal spectrum, we calculated the square roots of the FOMs at the contrast agent concentrations of 1 to 10 mg/mL for both iodine and gadolinium, and the results are shown in Fig. 16. It is a good approximation that the square roots of the FOMs are linearly dependent on the agent concentration. This can be explained by Eq. (21), where the term $F_{k,k}^{-1}$ is nearly independent of the agent concentration as long as the total attenuation is not significantly altered by the contrast agent itself. Hence, we would expect that the conclusions about the optimal spectrum vary little with change in the contrast agent concentration. The results in Fig. 16 also show that at the same concentration, the values of $\mathrm{SDNR}^2/\mathrm{BD}$ and $\mathrm{SDNR}^2/\mathrm{SD}$ in gadolinium imaging are, respectively, around 3 and 10 times larger than those in iodine imaging. From a physical point of view, gadolinium seems to be a better candidate in head imaging; however, from a physiological point of view, gadolinium is much more harmful to the human body than iodine.[53,54] In practice, the typical dose (mg) of gadolinium used for MRI is around 10 times less than that of iodine for CT imaging.[53,55] If such a difference in agent concentration is present in K-edge imaging, then the values of FOMs in the gadolinium imaging case, as illustrated in Fig. 16, are only 3% to 10% of those in the iodine imaging case. Nevertheless, which contrast agent is more suitable for head CT imaging is still an open question and remains to be answered in future researches by taking the toxicity and the damage to DNA into account.

Since silicon has a relatively low atomic number compared to other detector materials (such as cadmium and tellurium), Compton scattering plays an important role in our detector, as shown in Fig. 5(b). Although the resulting Compton events carry little spectral information, they might be beneficial to reduce the statistical noise in the images. To study how much gain we can get from the Compton events, we compared the FOMs with those obtained without including Compton events. The results show that with the optimal spectrum, the FOMs for nonenhanced imaging can be improved by 12% when Compton events are included. For K-edge imaging, the improvement is 3% in both iodine and gadolinium cases.

A number of limitations have to be noted. First, the arrangement of energy thresholds is not fully optimized, which to some extent underestimates the FOMs presented in this work. To gain some insight into the impact of this underestimation in our conclusions about the optimal spectrum for different imaging cases, we recalculated the FOMs by assuming that our detector has a large number of energy bins with 1-keV width. The results (circles in Fig. 14) show that the FOMs are little improved in nonenhanced imaging, while for K-edge imaging, a general improvement of 10% in the FOMs can be seen in both the iodine and gadolinium cases. However, little changes in the trend as a function of kVp are found in each imaging case. Therefore, we do not expect that the underestimation in FOMs due to the suboptimal arrangement of energy thresholds would change the conclusions on the optimal beam quality in this work. Second, only one blood vessel was considered in the head phantom. In practice, the contrast agents can be present in other blood vessels, which would greatly increase the radiation dose.[56] Recent findings[57,58] show that the additional secondary electrons produced when x-rays are absorbed by the contrast

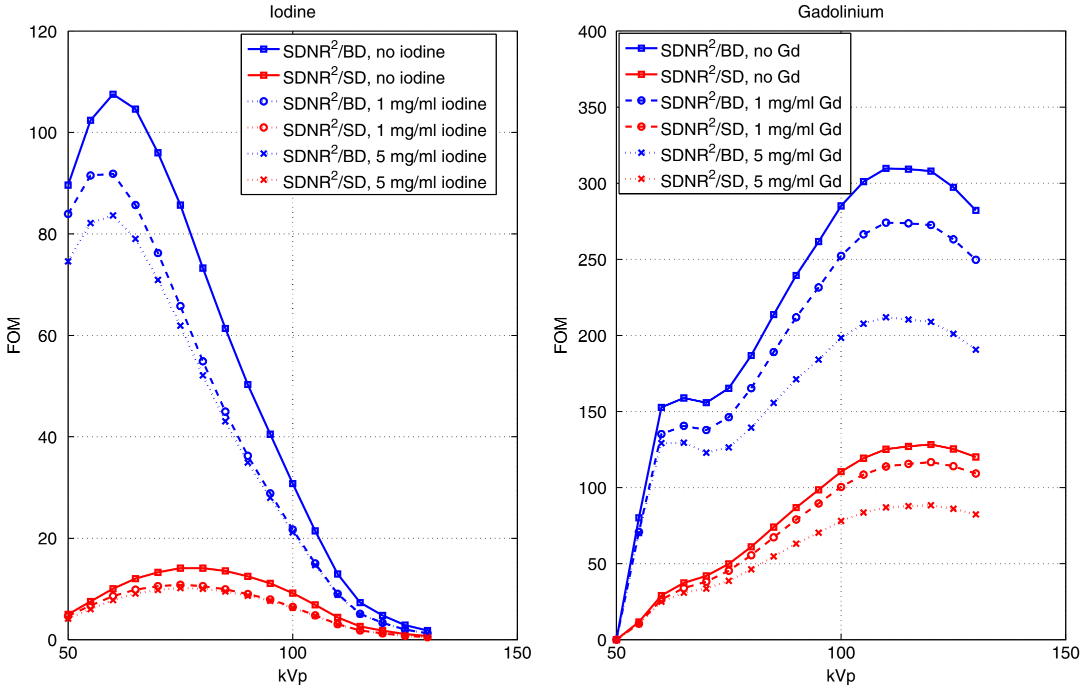

(a) (b)

Fig. 19 Resulting FOMs as a function of kVp when the contrast agents of two different concentrations, 1 mg/mL (circles) and 5 mg/mL (crosses), are present in the brain tissue, in comparison with those (squares) obtained without the contrast agents in the brain tissue. Note that the optimal filter of 2 HVL iodine is applied in (a) iodine imaging and (b) 2 HVL thulium in gadolinium imaging.

agents would lead to DNA damage. To investigate the effect of the dose increase on the spectrum optimization, we calculated the FOMs based on the assumption that the contrast agents are homogeneously distributed over the whole brain tissue in the head phantom. Two different contrast agent concentrations, 1 and 5 mg/mL, in the brain tissue were studied. The results (Figs. 17–19) show that although the presence of the contrast agents in the brain tissue decreases the FOMs, the optimal parameters (i.e., Z, l_Z, and kVp) remain almost the same for both iodine and gadolinium imaging. Furthermore, the diameter of the head phantom we studied is fixed. We redid the simulations with the head phantoms of diameters 10 cm (a size for pediatric applications) and 30 cm to evaluate whether the optimal spectrum is related to the size of the head phantom. The results show that the changes in this parameter cause little variation in the optimal spectrum settings for all imaging cases. Finally, although our study focuses on the detection of blood vessels, which is the common imaging task for acute stroke, the optimization methods described here can also be applied to other imaging applications, such as the detection of brain tumors and bones.

Acknowledgments

This study was supported by the Erling-Persson Family Foundation.

References

1. World Stroke Organization, "Stroke care," http://www.world-stroke.org/ (26 January 2015).
2. J. Mackay et al., *The Atlas of Heart Disease and Stroke*, World Health Organization, Geneva (2004).
3. American Stroke Association, "Ischemic strokes," http://www.strokeassociation.org/ (26 January 2015).
4. R. G. González et al., *Acute Ischemic Stroke*, Springer, Berlin, Germany (2011).
5. W. S. Smith et al., "Mechanical thrombectomy for acute ischemic stroke: Final results of the multi MERCI trial," *Stroke* **39**(4), 1205–1212 (2008).
6. R. G. Nogueira et al., "Trevo versus merci retrievers for thrombectomy revascularisation of large vessel occlusions in acute ischaemic stroke (trevo 2): a randomised trial," *Lancet* **380**(9849), 1231–1240 (2012).
7. D. S. Liebeskind et al., "Serial Alberta Stroke Program Early CT Score from baseline to 24 hours in solitaire flow restoration with the intention for thrombectomy study a novel surrogate end point for revascularization in acute stroke," *Stroke* **45**(3), 723–727 (2014).
8. A. Mnyusiwalla, R. I. Aviv, and S. P. Symons, "Radiation dose from multidetector row CT imaging for acute stroke," *Neuroradiology* **51**(10), 635–640 (2009).
9. M. Cohnen et al., "Radiation exposure of patients in comprehensive computed tomography of the head in acute stroke," *Ame. J. Neuroradiol.* **27**(8), 1741–1745 (2006).
10. M. E. Mullins et al., "CT and conventional and diffusion-weighted MR imaging in acute stroke: Study in 691 patients at presentation to the emergency department," *Radiology* **224**(2), 353–360 (2002).
11. A. Srinivasan et al., "State-of-the-art imaging of acute stroke 1," *Radiographics* **26**(suppl 1), S75–S95 (2006).
12. A. M. Allmendinger et al., "Imaging of stroke: part 1, perfusion ctoverview of imaging technique, interpretation pearls, and common pitfalls," *Am. J. Roentgenol.* **198**(1), 52–62 (2012).
13. K. Miles and M. Griffiths, "Perfusion CT: a worthwhile enhancement?," *Perfusion* **76**(904), 220–231 (2003).
14. Y. Imanishi et al., "Radiation-induced temporary hair loss as a radiation damage only occurring in patients who had the combination of MDCT and DSA," *Eur. Radiol.* **15**(1), 41–46 (2005).
15. A. B. Smith et al., "Radiation dose reduction strategy for CT protocols: Successful implementation in neuroradiology section 1," *Radiology* **247**(2), 499–506 (2008).
16. W. A. Kalender, H. Wolf, and C. Suess, "Dose reduction in CT by anatomically adapted tube current modulation. II Phantom measurements," *Med. Phys.* **26**(11), 2248–2253 (1999).
17. J. M. Boone and J. A. Seibert, "An accurate method for computer-generating tungsten anode x-ray spectra from 30 to 140 kv," *Med. Phys.* **24**(11), 1661–1670 (1997).
18. E. Samei et al., "A framework for optimising the radiographic technique in digital x-ray imaging," *Radiat. Prot. Dosim.* **114**(1–3), 220–229 (2005).
19. M. J. Tapiovaara and R. Wagner, "SNR and DQE analysis of broad spectrum x-ray imaging," *Phys. Med. Biol.* **30**(6), 519 (1985).
20. J. Giersch, D. Niederlöhner, and G. Anton, "The influence of energy weighting on x-ray imaging quality," *Nucl. Instrum. Methods Phys. Res. Sec. A* **531**(1), 68–74 (2004).
21. P. M. Shikhaliev, "Projection x-ray imaging with photon energy weighting: experimental evaluation with a prototype detector," *Phys. Med. Biol.* **54**(16), 4971 (2009).
22. T. G. Schmidt, "CT energy weighting in the presence of scatter and limited energy resolution," *Med. Phys.* **37**(3), 1056–1067 (2010).
23. P. M. Shikhaliev, "Beam hardening artefacts in computed tomography with photon counting, charge integrating and energy weighting detectors: a simulation study," *Phys. Med. Biol.* **50**(24), 5813 (2005).
24. R. E. Alvarez and A. Macovski, "Energy-selective reconstructions in x-ray computerised tomography," *Phys. Med. Biol.* **21**(5), 733 (1976).
25. J. Schlomka et al., "Experimental feasibility of multi-energy photon-counting k-edge imaging in pre-clinical computed tomography," *Phys. Med. Biol.* **53**(15), 4031 (2008).
26. E. Roessl and R. Proksa, "K-edge imaging in x-ray computed tomography using multi-bin photon counting detectors," *Phys. Med. Biol.* **52**(15), 4679 (2007).
27. C. Xu et al., "Evaluation of a second-generation ultra-fast energy-resolved asic for photon-counting spectral CT," *IEEE Trans. Nucl. Sci.* **60**(1), 437–445 (2013).
28. X. Liu et al., "A silicon-strip detector for photon-counting spectral CT: energy resolution from 40 kev to 120 kev," *IEEE Trans. Nucl. Sci.* **61**(3), 1099–1105 (2014).
29. H. Bornefalk et al., "Effect of temperature variation on the energy response of a photon counting silicon CT detector," *IEEE Trans. Nucl. Sci.* **60**(2), 1442–1449 (2013).
30. H. Bornefalk and M. Danielsson, "Photon-counting spectral computed tomography using silicon strip detectors: a feasibility study," *Phys. Med. Biol.* **55**(7), 1999 (2010).
31. M. Persson et al., "Energy-resolved CT imaging with a photon-counting silicon-strip detector," *Proc. SPIE* **9033**, 90333L (2014).
32. A. Macovski et al., "Energy dependent reconstruction in x-ray computerized tomography," *Comp. Biol. Med.* **6**(4), 325–336 (1976).
33. M. Firsching et al., "Quantitative material reconstruction in CT with spectroscopic x-ray pixel detectors–a simulation study," in *Nuclear Science Symposium Conference Record*, Vol. 4, pp. 2257–2259, IEEE, San Diego, California (2006).
34. J. P. Ronaldson et al., "Toward quantifying the composition of soft tissues by spectral CT with medipix3," *Med. Phys.* **39**(11), 6847–6857 (2012).
35. E. Roessl and C. Herrmann, "Cramér-Rao lower bound of basis image noise in multiple-energy x-ray imaging," *Phys. Med. Biol.* **54**(5), 1307 (2009).
36. K. M. Hanson, "Detectability in computed tomographic images," *Med. Phys.* **6**(5), 441–451 (1979).
37. H. Bornefalk and M. Persson, "Theoretical comparison of the iodine quantification accuracy of two spectral CT technologies," *IEEE Trans. Med. Imaging* **33**(2), 556–565 (2014).
38. M. Tapiovaara and R. Wagner, "SNR and noise measurements for medical imaging: I. A practical approach based on statistical decision theory," *Phys. Med. Biol.* **38**(1), 71 (1993).
39. M. Yveborg, M. Persson, and H. Bornefalk, "Optimal frequency-based weighting for spectral x-ray projection imaging," *IEEE Trans. Med. Imaging* **34**(3), 779–787 (2015).
40. A. E. Burgess, F. L. Jacobson, and P. F. Judy, "Human observer detection experiments with mammograms and power-law noise," *Med. Phys.* **28**(4), 419–437 (2001).
41. H. H. Barrett and K. J. Myers, "Foundations of image science," *Foundations of Image Science*, H. H. Barrett and K. J. Myers, Vol. **1**, pp. 1584, Wiley-VCH, New York (2003).

42. L. Lehmann et al., "Generalized image combinations in dual KVP digital radiography," *Med. Phys.* **8**(5), 659–667 (1981).
43. S. Riederer and C. Mistretta, "Selective iodine imaging using K-edge energies in computerized x-ray tomography," *Med. Phys.* **4**(6), 474–481 (1977).
44. L. Lehmann and R. Alvarez, "Energy-selective radiography a review," in *Digital Radiography*, pp. 145–188, Springer, New York (1986).
45. M. J. Berger et al., "Xcom: photon cross sections database," *NIST Stand. Ref. Database* **8**(1), 3587–3597 (1998).
46. C. Xu et al., "Energy resolution of a segmented silicon strip detector for photon-counting spectral CT," *Nucl. Instrum. Methods Phys. Res. Sec. A* **715**, 11–17 (2013).
47. U. S. Food and Drug Administration (FDA), "Diagnostic x-ray systems and their major components," *Code Fed. Reg.* 21 CFR(1020.33) (1984).
48. G. Santin et al., "GATE: A Geant4-based simulation platform for PET and SPECT integrating movement and time management," *IEEE Trans. Nucl. Sci.* **50**(5), 1516–1521 (2003).
49. J. A. Bauhs et al., "CT dosimetry: comparison of measurement techniques and devices 1," *Radiographics* **28**(1), 245–253 (2008).
50. J. T. Dobbins et al., "Chest radiography: optimization of x-ray spectrum for cesium iodide–amorphous silicon flat-panel detector 1," *Radiology* **226**(1), 221–230 (2003).
51. M. Yveborg, M. Danielsson, and H. Bornefalk, "Performance evaluation of a sub-millimetre spectrally resolved CT system on high- and low-frequency imaging tasks: a simulation," *Phys. Med. Biol.* **57**(8), 2373 (2012).
52. R. E. Alvarez, "Near optimal energy selective x-ray imaging system performance with simple detectors," *Med. Phys.* **37**(2), 822–841 (2010).
53. U. Nyman et al., "Are gadolinium-based contrast media really safer than iodinated media for digital subtraction angiography in patients with azotemia?," *Radiology* **223**(2), 311–318 (2002).
54. J. C. Weinreb, "Which study when? Is gadolinium-enhanced MR imaging safer than iodine-enhanced CT?," *Radiology* **249**(1), 3–8 (2008).
55. M. R. Prince, C. Arnoldus, and J. K. Frisoli, "Nephrotoxicity of high-dose gadolinium compared with iodinated contrast," *J. Magn. Res. Imaging* **6**(1), 162–166 (1996).
56. E. Amato et al., "A method to evaluate the dose increase in CT with iodinated contrast medium," *Med. Phys.* **37**(8), 4249–4256 (2010).
57. E. I. Piechowiak et al., "Intravenous iodinated contrast agents amplify DNA radiation damage at CT," *Radiology* **275**(3), 692–697 (2015).
58. A. B. de Gonzalez and R. A. Kleinerman, "CT scanning: is the contrast material enhancing the radiation dose and cancer risk as well as the image?," *Radiology* **275**(3), 627–629 (2015).

Han Chen is a PhD student at the University of Royal Institute of Technology (KTH) in Sweden.

Cheng Xu works as a postdoc at Royal Institute of Technology (KTH) in Sweden.

Mats Persson is PhD student at Royal Institute of Technology (KTH).

Mats Danielsson is professor of the Department of Physics in Royal Institute of Technology (KTH). He is also CEO of Prismatic Sensors AB, a company commercializing a new technology for photon counting CT.